Rupture Process of the April 18, 1906 California Earthquake from near-field Tsunami Waveform Inversion

Stefano Lorito[1*], Alessio Piatanesi[1] and Anthony Lomax[2]

[1] *Istituto Nazionale di Geofisica e Vulcanologia, Department of Seismology and Tectonophysics, Via di Vigna Murata 605, 00143 Rome, Italy*
[2] *ALomax Scientific, Mouans-Sartoux, France*, www.alomax.net
* corresponding author, e-mail address lorito@ingv.it

Abstract

The April 18, 1906 M8 California earthquake generated a small local tsunami that was recorded in the near-field by the Presidio, San Francisco tide-gage, located near the Golden Gate. We investigate the causative, tsunamigenic seismic source by forward modeling and nonlinear inversion of the Presidio marigram. We use existing seismological and geological observations to fix the fault system geometry and the surface slip on the onland portions of the San Andreas fault (SAF). We perform synthetic inversions to show that the single, near-field marigram constrains the main features of the rupture on the portion of the SAF system offshore of the Golden Gate. Finally we perform nonlinear inversions for the slip distribution and the timing of the rupture of the 1906 earthquake.

Our results, in agreement with previous studies, identify a dilatational step-over and show a bi-lateral rupture, possibly originating or propagated through the step-over region. We find that little or no co-seismic slip on normal faults in the step-over region is required to fit the marigram, and we obtain adequate fits when allowing delays in the source initiation times of up to 3 minutes on the various fault segments. We constrain slip to be of about 5-6 meters for the onshore portion of the SAF to the northwest of the Golden Gate, in agreement with 1906 surface observations of fault offset. Our results favour the hypothesis of a vertical dip

for a currently aseismic SAF to the southeast of the Golden Gate, under the San Francisco Peninsula.

Introduction

Inversion of tsunami waveforms has long been known to be a valid technique for retrieving information about the causative earthquake source, since the seminal paper of Satake (1987). It has been shown that tide-gage records and run-up heights are useful to constrain some earthquake source parameters. In particular, they have good resolving power of the spatial extent and slip distribution for a tsunamigenic earthquake (Johnson et al., 1996; Piatanesi et al., 1996; Geist, 1999; Ortiz and Bilham, 2003). Recently, tide-gage data have also been used for retrieving rise-time and average rupture propagation, both with a linear inversion technique by Fujii and Satake (2006, 2007), and with a nonlinear technique which retrieves simultaneously slip amplitudes and rupture velocity (Piatanesi and Lorito, 2007).

The 18 April 1906 California earthquake caused a large number of deaths and much damage, but it generated only a moderate tsunami, characterized mainly by a lowering of the sea-level of about 10 cm. The tsunami was recorded by the Presidio tide-gage in San Francisco, as described by the report of Lawson (1908). The ground-shaking hazard in the San Francisco bay region is considered much higher than tsunami hazard, because of the predominantly horizontal motion of the causative, strike-slip faults. Conversely, the Presidio marigram has been analysed in comparison to tsunami models by a few authors, with the aim of constraining features of the 1906 earthquake rupture and of the nearby portion of the offshore San Andreas fault (SAF). Ma et al. (1991), by linear least square inversion, retrieved a subsidence pattern associated with the right-stepping bend of the SAF, just offshore from

the Golden Gate, and consistent with a horizontal strike-slip of 5-6 m. More recently, Geist and Zoback (1999, 2002) have modeled the tsunami generated by several scenarios of rupture and corresponding subsidence, showing that the 1906 marigram is compatible with a dilatational step-over and a bi-lateral rupture, possibly originating or propagated through the step-over region. Though the record is a single point observation, its location in the near-field of the faulting structures that ruptured during the 1906 earthquake makes the Presidio marigram suitable for retrieving useful information about the seismic source.

Lomax (2007) defines a likely focal volume for the 1906 earthquake, overlapping the step-over (or bend) in the submerged fault system offshore of the Golden Gate. He also defines, on the basis of present day seismicity, three major faulting structures around the likely focal volume (Figure 1). The first is a steeply south-west dipping structure under the northern San Francisco Peninsula segment of the SAF exhibiting present-day normal faulting, hereafter named SFP structure or simply SFP. The second is a west-dipping structure under the Golden Gate Platform, summarizing a complex zone of predominantly normal faulting or deformation (hereafter WSF). The third is a strike-slip structure to the northwest, along the SAF zone (NWSAF). Lomax (2007) also proposes temporal scenarios for the bi-lateral rupture.

We use these faulting structures as a starting source geometry to numerically simulate the tsunami generated by the 1906 San Francisco earthquake and to perform nonlinear inversions, with the aim to simultaneously retrieve source slip distribution and timing of the rupture. We indeed include the possibility of a delayed rupture on NWSAF and/or SFP, to test different rupture timing scenarios.

1906 Presidio tide-gage tsunami record

The tsunami generated by the April 18, 1906 earthquake was recorded by the Presidio tide-gage at Fort Point, beneath the present day Golden Gate bridge. The functioning of the standard automatically recording tide-gage is accounted in detail by Bowditch (1966). The marigram plot published and discussed by Lawson (1908) is shown in Figure 2. The arrow indicates a blur just after 5 a.m., caused by the intense shaking. The beginning of the blur is generally accepted as roughly corresponding to the earthquake origin time, while the width of the blur may correspond to the duration of the strong motion at Fort Point .

We have scanned the marigram image and digitized it accurately. We then removed the low frequency tidal contribution from the tide-gage record, as tsunami simulation does not include tides. The tsunami was recorded during an increasing tide level. We analyze the first hour of record after the earthquake, which is centered around the middle point between low and high tide. To extract the tsunami signal, we subtracted from the observed marigram the linear trend that we estimated from the two hours of recordings prior to the earthquake. This detrended marigram is shown in the upper panel of Figure 3. It shows a first small depression of a few centimeters amplitude between 3 and 9 minutes after the earthquake. It later shows a second deeper depression (>10 cm), starting at about 9-10 minutes and recovering after about 25 minutes. The amplitude of the higher frequency oscillations superposed on both the marigram depressions is comparable to those of the oscillations that preceed the earthquake.

We calculate the continuous wavelet transform power spectrum of the detrended marigram, making use of the Morlet wavelet. For details on wavelet analysis and Morlet wavelet see Grinsted et al.(2004) or Torrence and Compo (1998), and references therein. The wavelet power spectrum of the detrended record is shown in Figure 3, lower panel. It represents the evolution with time of the spectral power, at the different periods spanned by the scale on the vertical axis. The thick black contours fix the 95% confidence level. It has

been calculated by assuming a red-noise background model, and by estimating its governing autocorrelation coefficient by the marigram itself. The spectral power values below the confidence level are thus likely to be spectral expression of the noise. The higher values (darker regions) inside the confidence contours are likely to be true signal. Moreover, everything above the dashed line is to be disregarded as likely corrupted by edge effects.

We notice that significant energy is present before the earthquake origin time, and with periods roughly comprised between 4 and 16 minutes. Such a spectral feature has been previously ascribed to metereological effects (Geist and Zoback, 2002), and observed for about two days before the earthquake (Disney and Overshiner, 1925). A ridge in the spectral energy (indicated by an arrow in Figure 3) forms at about 9.5 minutes. It reveals a sudden change in the marigram timeseries and could indicate the arrival time of the main tsunami signal. This is consistent with a simple analysis of the water wave travel-times from the Presidio tide-gage, shown in Figure 4. The travel-times have been calculated using the long-wave linear shallow water approximation for phase velocity $c=sqrt(gh)$, where g is the Earth's surface gravitational acceleration and h is the water depth. The contour line at 9 minutes roughly intersects the edge of the considered fault system (see Figure 1), just southeast of the Golden Gate. The cone of influence corresponding to the ridge in the wavelet spectrum expands progressively, with increasing period and contains energy in the tsunami band, that is from 7-8 minutes up to 30 minutes.

As the band of the meteorological and tsunami signals appear to overlap, particularly with regard to the early depression prior to 10 minutes, it is difficult to assess the origin of this sea level variation. It could contain both wind-generated waves and tsunami waves of relatively low amplitude generated by local coseismic displacement within the 5 minute travel-time contours (Figure 4). Accordingly, tsunami waves as well as wind waves both contains frequencies associated with local bathymetry and topography and so it is not a simple

task to distinguish between them (Rabinovich, 1977). Nevertheless, it is likely that the tsunami arrival progressively disrupts the preexisting meteorological effects (Geist and Zoback, 2002), and then the second larger depression (past 10 minutes) can be interpreted as a true tsunami wave recording.

Hydrodynamic modeling

Tsunamis are considered long shallow-water gravity waves, since their wavelength is usually much larger than the sea depth. In this study we use the nonlinear shallow water equations written as follow:

$$\begin{cases} \dfrac{\partial(z+h)}{\partial t} + \nabla \cdot \left[\mathbf{v}(z+h)\right] = 0 \\ \dfrac{\partial \mathbf{v}}{\partial t} + (\mathbf{v} \cdot \nabla)\mathbf{v} = -g\nabla z + \mathbf{C} + \mathbf{F} \end{cases} \qquad (1)$$

In eqs.(1), z represents the water elevation above sea level, h the water depth in a still ocean, $\mathbf{v}$ the depth-averaged horizontal velocity vector, g the gravity acceleration, and $\mathbf{C}$ and $\mathbf{F}$ represent the Coriolis and bottom friction forces respectively. The boundary conditions are pure wave reflection at the solid boundary (coastlines) and full wave transmission at the open boundary (open sea). The equations are solved numerically by means of a finite difference method on a staggered grid (Mader, 2001). The time of coseismic displacement can be neglected and the initial seawater elevation is assumed to be equal to the coseismic vertical displacement of the sea bottom, computed through the Okada's analytical formulas (Okada, 1992), while the initial velocity field is assumed to be identically zero. We run each simulation of this study to model 60 minutes of tsunami propagation, in a rectangular domain

(123 to 122°W, 37.25 to 38°N) with 3 arc-second (~93 meters) of spatial resolution, using the NGDC Coastal Relief Model bathymetric dataset (Divins and Metzger, available at http://www.ngdc.noaa.gov/mgg/coastal/coastal.html). The computational domain is shown in Figure 1 along with the bathymetry and topography. The resolution of the dataset is sufficient to accurately model at least the leading tsunami waves, both in amplitude and phase. Due to the assumption of total reflection along the coastlines and to eventually unmodeled short-wavelength coastline features, some high frequency features of the tsunami waveform are likely to be less accurately modeled.

The simulated marigrams are the difference between the water level time evolution and the coseismic vertical displacement; this is the actual quantity a real tide-gage would measure, neglecting earthquake shaking and assuming that the coseismic displacement time scale is much shorter than the time required for the gravitational equilibrium to be restored by water wave propagation.

Forward modeling of the 1906 tsunami

We first perform forward tsunami modeling using the three fault structures shown in Figure 1. As an initial condition we impose the sea-floor displacement plotted in Figure 5. It corresponds to 5 m of slip on the NWSAF segment, 4 m of slip on the SFP segment, both with a strike slip (right lateral) mechanism (respectively dip 90° and 75°), and 1 meter on the WSF segment (dip 65°, normal). We recall that slip on NWSAF and SFP (on land, away from the step-over) has been constrained by observations related to the 1906 earthquake and more recent teleseismic and geodetic waveform modeling (Lawson, 1908; Wald et al., 1993; Thatcher et al., 1997; Kenner and Segall, 2003; Song et al., 2007), while the geometry of the

faults is inferred by Geist and Zoback (2002, and references therein), by Zoback et al. (2002) and by Lomax (2007), who introduces the WSF structure.

We simulate the propagation of the tsunami generated by the assumed slip distribution, and analyze the time evolution of the sea-level height (marigram) at the position of the tide-gage. In Figure 6a, we show both the simulated marigram and the 1906 tide-gage record. Compared to the 1906 record, the simulated marigram shows a too early and broad sea-level depression, starting at about 8-10 minutes after the earthquake and with a positive polarity phase reaching its maximum at about 23 minutes. The marigram subsequently settles around a negative base-line value, consistent with the positive vertical displacement experienced by the San Francisco Peninsula (Figure 5).

The earlier depression in the marigram can be partly due to the contribution of the displacement on WSF, as the plot of Figure 6b indicates. It shows the simulated marigram generated with a slip of 1 m on WSF only, and with zero slip both on NWSAF and SFP. The earlier marigram depression could also due to displacement caused by slip at or near the ends of the NWSAF and SFP segments, and around the step-over between those two segments, and also suggests the hypothesis of a few-minutes delayed rupture initiation on some of the structures (Lomax, 2007).

Some authors propose a steeper southwestward dip of the SAF at the location of our SFP segment along the San Francisco Peninsula (Parsons et al., 2002; Zoback et al. 1999) or even a northeastward dip of the SAF beneath the San Francisco bay toward the Hayward Fault (Parsons and Hart, 1999). We test the effect of changing the dip angle of SFP to vertical (90°), with the same slip configuration we started forward modeling with (5 m slip on NWSAF, 1 m on WSF and 4 m on SFP). The effect of a steeper SFP is shown in Figure 6c, where a slight improvement of the agreement between the two marigrams is apparent for the later phases (after 30 minutes) while the match remains unchanged in the first 30 minutes.

205

Non linear inversion of the 1906 Presidio tide-gage record

Method

210

To better constrain the 1906 earthquake source parameters, we follow the approach proposed by Piatanesi and Lorito (2007) which combines classical Green's functions methods with a nonlinear global search inversion technique.

We model the NWSAF, WSF and SFP structures as three, rectangular, planar faults, and
215 divide the ends of the NWSAF and SFP faults into 6 and 5 rectangular subfaults respectively (Figure 1). Including WSF, we then obtain a set of 12 subfaults, whose parameters are listed in Table 1. We hold the rake on NWSAF and SFP fixed to 180° and the rake on WSF to 270°, whilst in some cases we test two dip angles (75 and 90°) on the NWSAF structure.

For each of the 12 subfaults, we use a nonlinear shallow water approximation to
220 calculate the marigrams corresponding to unitary slip (Green's functions) at the coordinates of the Presidio tide-gage. At this stage we use a linear approximation, to obtain synthetic marigrams by linear combination of the individual subfaults contribution.

The observed marigram exhibits only moderate amplitude and it is recorded at a near-field tide-gage. To test if the linear approximation holds in this particular situation, we
225 compare two simulated marigrams, the first obtained as a linear combination of the Green's functions, and the second calculated with a composite 12 subfaults source (Figure 7). The agreement between the marigrams is almost perfect from 0 to 20-25 minutes, but slightly worsens for the later phases, which nevertheless have comparable average value and amplitude/frequency of the oscillations around the mean values. The variance of the residuals

between the two marigrams is less than 2% of the variance of the marigram generated by the source as a whole, and considering the timeseries past 25 minutes. We will later take this into account when we perform synthetic tests with added noise with a variance of 10% of the time series variance.

The observed and synthetic waveforms are compared in the time domain, through an objective cost function that is a hybrid representation between L_1 and L_2 norm (Spudich and Miller, 1990; Sen and Stoffa, 1991), that can be written as:

$$E(m) = 1 - \frac{2\sum_{t_i}^{t_f}(u_O(t)u_S(t))}{\sum_{t_i}^{t_f}u_O^2(t) + \sum_{t_i}^{t_f}u_S^2(t)} + C \qquad (2)$$

In eq. (2) u_O and u_S are the observed and synthetic waveforms respectively, t_i and t_f are the lower and upper bounds of the time window. C is a schematic representation of constraints included into the cost function. Such a cost function exploits information from both the shape and the amplitude of a waveform and it is more robust than the standard least squares technique.

In this work, we invert for the slip distribution over the set of 12 subfaults. To test for the temporal rupture scenarios proposed by Lomax (2007), we allow for a delay of the slip on either the SFP or NWSAF subfaults subset. Simultaneously inverting for both slip and delay leads to a nonlinear inverse problem (Beresnev, 2003; Piatanesi and Lorito, 2007).

To deal with this problem, we use a global optimization method that is a particular implementation of the simulated annealing technique, called the “heat bath algorithm” (Rothman, 1986). This technique, already used in non-linear finite fault inversion (e.g. Ji et al., 2002; Liu and Archuleta, 2004), performs a large sampling of the model space and

concentrates the search on regions characterized by low values of the cost function, i.e., where the optimal models are likely to be found.

Synthetic tests, source parameters and constraints

We investigate the resolution of our inversion problem with a target synthetic marigram constructed by combining the Green's function according to several imposed known slip configurations. The inversions produce a very good reconstruction of the target marigram, but do not retrieve all the details of the target slip configuration, particularly on the southernmost subfault of SFP (subfault 12 on Figure 1). We conclude that the problem is over-parametrized, and we need to a-priori impose some of the parameters values before inverting for the slip in the 1906 earthquake case.

We then fix the slip on subfault 12 to 4 meters, consistently with surface observations (Lawson, 1908; Wald et al., 1993; Thatcher et al., 1997; Kenner and Segall, 2003; Song et al., 2005). We moreover impose a very simple smoothing constraint to the ends of the NWSAF and SFP structures. We allow for variation of slip on the terminal subfaults 1 and 6 on NWSAF, and calculate the slip on intermediate faults 2 to 5 as a linear interpolation of the slip on 1 and 6. We do the same on SFP, retaining only the slip on subfault 8 as a free parameter, since the slip on subfault 12 is fixed to 4 m. We thus reduce our problem to 4 free slip parameters (i.e., slip on subfaults 1,6,7 and 8), and perform a further synthetic test to check the effectiveness in inverting for both the slip distribution and the timing of the rupture initiation.

We build a test rupture model that consists of the slip values on the subfaults shown by the circles in Figure 8b. Rupture on NWSAF is assumed to be delayed 3 minutes. The Green's functions are then linearly combined and delayed according to the imposed rupture properties.

The resulting waveform is then corrupted by adding a Gaussian random noise with a variance that is 10% of the clean waveform amplitude variance (Ji et al., 2002; Piatanesi and Lorito, 2007). The target waveform is shown in Figure 8a. The artificial noise level we introduce is much greater than the estimated errors introduced by the linear approximation. It is also greater than the background noise in the Presidio tide-gauge record, estimated from the time series before the first tsunami arrival.

We introduce a priori information on the model solution by imposing lower and upper bounds to the range of possible source parameters, namely 0-10 m for the slip amplitude on the NWSAF subfaults set, 0-4 m on the WSF subfault and 0-8 m on the SFP subset, with the exception of the subfault 12, fixed at 4 m. We also define a range of 0 to 6 minutes for the rupture initiation delay on NWSAF.

The inverted marigram is plotted in Figure 8a. It closely follows the target one, irrespectively of the noise added. Also plotted is an ensemble of good models retrieved during the minimum (best model) search, that is the models with a probability that is at least the 95% of the best model probability.

The best inverted model is very similar to the target one: the slip distribution along the three structures is almost exactly reproduced (Figure 8b). In any of the cases the target slip lies inside the 1 σ error bars defined by the single parameters standard deviation in the above 95% good models class. It should be noted that the standard deviations of the interpolated parameters, that is subfaults 2 to 5 and 9 to 11, are derived by interpolating those of the terminal parameters (1,5 and 8,12 respectively). It is then just an indication of the slip variability on the intermediate subfaults associated with errors on terminal subfaults. We moreover find a best model delay of 3 minutes, that is then coincident with the target one, and with a standard deviation of 1.16 minutes.

Figure 8c shows the marginal distributions of each parameter, including rupture initiation delay, for the good models ensemble. The black lines represent the best model values. Both standard deviations of Figure 8b and marginal distributions of Figure 8c give a measure of the uncertainties in the estimation of the corresponding parameter. Smaller values of the standard deviation (as well as more peaked marginals) indicate that the corresponding parameters are better resolved than those characterized by larger deviations (Mosegaard and Tarantola, 1995; Sambridge and Mosegaard, 2002; Piatanesi and Lorito, 2007). In the present case the marginals are single-peaked and centered around the best model, thus well representing the ensemble of good models, as a result of a likely weakly nonlinear problem. The results of the synthetic test then allow to apply the inversion to infer rupture properties of the 1906 earthquake by means of the Presidio marigram.

Application to the 1906 earthquake

We perform inversions with a dip of both 75° and 90° on the SFP structure and, confirming the results of forward modeling, we find a better agreement with the Presidio marigram with the steepest dip 90° SFP fault. The inverted marigrams for the 75° and 90° cases are shown in Figure 9a and 9b respectively. Both show a slightly early arrival of the broader minimum compared to that of the Presidio marigram. We thus investigate three temporal scenarios, with the goal of reproducing the early arrival of the broader minimum. The first temporal scenario allows delayed rupture initiation on SFP with respect to WSF and NWSAF. The second scenario allows simultaneous delay of both SFP and NWSAF ruptures with respect to that on WSF. The third scenario allows for delayed rupture initiation on NWSAF with respect to SFP and WSF.

The inversion results lead to the rejection of the first scenario, indicating that no delay is allowed on SFP alone. For the second scenario we obtain exceedingly high slip on the inland portion of NWSAF, so we fix this slip parameter to a value of 6 meters, consistent with the observed 1906 surface offset. This gives the marigram shown in Figure 10a that has a fairly good fit with the observed Presidio marigram. However, examination of the full inversion results shows a trade-off between the slip values on the WSF structure (up to a maximum of 20 cm) and delayed slip on SFP northwestern end (1-2 meters). In other words, as the delay on NWSAF and SFP varies, we find a class of comparably good models with either slip on WSF and a delay <3 minutes or no slip on WSF and a delay >3 minutes.

The marigram produced by the nonlinear inversion for the third temporal scenario, resolving a 3 minute delay on NWSAF, is shown in Figure 10b. This is the best fitting marigram retrieved by our inversions for the 1906 earthquake. Our results thus weakly favour the third temporal scenario, and we further examine this case in the next subsections.

We find that there is a relatively large uncertainty (a few minutes) on the inversion results for the delay value, particularly when allowing delay on SFP. Moreover, some trade-off exists between the delay of the rupture and the position of the northwestern end of SFP, since the travel times to the Presidio tide gauge depend on both of these parameters. In contrast, the delay of the NWSAF rupture is less dependent on this trade-off since the subfaults at its southeastern end run roughly parallel to the 9 minutes travel-time contour (see Figure 4). The delay on NWSAF is a common feature of both the second and the third temporal scenario. However, it is not possible to completely rule out a scenario where both SFP and NWSAF rupture with the same delay, as this produces a sufficiently good fit to the marigram, although within the uncertainties discussed above.

Given these results, we examine below in greater detail the inversion results for the 1906 earthquake rupture obtained with the following model:

i) 4 metres fixed slip on SFP inland (and linear smoothing);

ii) 90° dip on SFP;

iii) delayed rupture on NWSAF.

The results of the inversion are summarized in Figure 11. The observed marigram lies almost entirely in the band defined by the ensemble of good models (Figure 11a), with the exception of the first negative peak at about 6 minutes and the first positive at 10 minutes, that are at the edge of the good models band. The best model is also a reasonable reproduction of the gross features of the Presidio marigram. Figure 11b shows the inverted best model slip values on the three structures, along with 1 σ error bars. Again, as in the synthetic test case, errors on intermediate subfaults are derived from errors on the terminals. The marginal distributions of each parameter for the ensemble of good models are plotted as histograms in Figure 8c, they show that all free parameters are well constrained. Retrieved slip values with standard deviations are also reported in Table 1.

The retrieved rupture initiation delay on NWSAF is 3 minutes, with a standard deviation of 0.44 minutes. Little or no slip is required on WSF faults, at least to accommodate constraints posed by the gross features of the Presidio marigram. The synthetic test above nevertheless showed that we have sufficient resolution to estimate slip on WSF, if present (Figure 8c). The retrieved slip value for the onland part of the NWSAF structure is consistent with the observed 1906 surface offset.

In Figure 12, we show the static displacement generated by the inverted slip distribution. It is similar to the displacement for our forward model (Figure 5) with regards to uplift under San Francisco Peninsula and the main subsidence lobe, but includes a zone of subsidence extending northward along the NWSAF structure. Relative to the forward results, the westernmost uplift lobe is displaced to the south east, near Daly city, and now roughly matches the topography around the SAF.

Discussion and conclusions

We have investigated the slip distribution and the time evolution of the 1906 April 18 California earthquake through forward and inverse modeling.

We constrain the main features of the seismic source using the sea-level height recorded at the Presidio tide-gage during the first hour following the earthquake. We also employ surface observations and seismological information related to the 1906 earthquake to better constrain the inversion problem. In particular, on the basis of recent literature (e.g. Geist and Zoback, 2002; Lomax ,2007), we use a fault geometry consisting of three main structures, namely NWSAF, WSF and SFP; then we divide the NWSAF and SFP structures into several sub faults to allow tapered slip at their ends With this geometry, we perform synthetic tests to assess the resolution of the problem, showing that a single marigram, in the near-field with respect to the seismic source, constrains the main features of the rupture on the portion of the SAF system offshore of the Golden Gate.

The best fitting model is characterized by variable slip on the subfaults, the largest slip occurring on the northernmost stretch of the NWSAF segment and decreasing from 5.7 to 2.3 meters along the structure in the southward direction. The slip on the WSF segment is found to be nearly absent. The slip on SFP increases from 0 to 4 meters going towards the southeast onland portion of SFP. We obtain the best inversion results with a delayed rupture on NWSAF with respect to the SFP.

Our results are in good agreement with previous results for the 1906 earthquake. Models of the 1906 earthquake rupture based on geodetic and seismic data (e.g. Thatcher et al., 1997; Ward, 2000; Song et al., 2007) show a grossly similar slip pattern, with the highest slip to the

northwest of the Golden Gate (NWSAF structure) and less slip to the southeast of the Golden Gate (SFP structure). Our results are also consistent with the scenarios proposed by Geist and Zoback (1999, 2002) and by Lomax (2007) which include a dilatational step-over offshore the Golden Gate. Geist and Zoback (1999, 2002) also consider a small compressional step-over in the SAFZ in the northern part of the Golden Gate platform, near Bolinas. We do not examine this case in our modeling, since we obtain good fitting with a simpler geometry. Our results are consistent with a bilateral rupture originating in the step-over region between SFP and NWSAF; this kind of rupture initiation has been already observed during other predominantly strike-slip earthquakes, such as the November 12, 1999 Duzce (e.g. Duman et al. 2005) or the January 17, 1995 Kobe earthquakes (e.g. Spudich et al., 1998).

We can only weakly constrain the timing of the rupture initiation on the NWSAF and SFP segments, as we have a better resolving power on the slip amplitude than on the temporal delay. The inversion results rule out a delay of the rupture on SFP only, and we find a trade-off between delay on SFP and slip on WSF when delay on both SFP and NWSAF are allowed. Conversely, a delay of about 3 minutes on the NWSAF structure is a robust feature of the best models, though it is inferred with a rough resolution, also of 3 minutes. One explanation for this feature could be delayed rupture triggering in the near field driven by static and dynamic stress interaction (e.g. Steacy et al., 2005, and references therein), although further resolution of this issue beyond the scope of our study.

Delayed rupture on the NWSAF is consistent with one of the three scenarios proposed by Lomax (2007), although Lomax (2007) prefers rupture initiation on the NWSAF segment because this segment is the locus of the largest 1906 surface rupture and it overlaps most the likely 1906 hypocenter location, and because the SFP structure shows present-day extensional tectonism and thus may have low confining stresses. In addition, we cannot exclude a delayed rupture on both the NWSAF and SFP segments. In this case, it would be possible that a

relatively small normal displacement (up to 20 cm) in the extensional step-over region triggered delayed rupture on the adjacent structures.

The marigram record also constrains the SFP segment to have a vertical or steeper than 75° dip angle, in agreement with some previous results (e.g., Parsons et al., 2002). The inference of a 75° dip angle as well as the 70° dipping WSF patch associated with normal faulting are both based on present day seismicity (e.g., Lomax, 2007). Since our inversions identify little or no slip occurred on the WSF structure during the 1906 earthquake and favour a vertical SFP, our results support the suggestion of Zoback et al. (1999), that the SAF is currently in a locked state and most of the current seismicity occurs on secondary faults adjacent to the SAF itself.

Nevertheless the patterns of observed, recent micro-seismicity and the difficulties in fitting the observed Presidio marigram indicate the need for more complex and complete modeling of the step-over region, perhaps involving oblique strike-slip and normal faulting or faulting on many smaller faults that fill a volume (e.g. Parson et al., 2003; Lomax 2007). Accordingly, an important issue in near-field tsunami modeling is the source complexity (e.g., Geist, 2002). Ideally, further modeling should avoid many of the simplifying assumptions generally made for seismogenic tsunami modeling, such as the use of an elastic half-space, or simple, planar faulting structures. Moreover, a thorough spectral separation of the source signal from local bathymetric effects could allow for more accurate modeling of the marigram. Such modeling may resolve some of the ambiguities and contradictions in the current understanding of the 1906 rupture near San Francisco, providing additional information for the assessment of seismic hazard in the San Francisco Bay area.

Acknowledgements

We acknowledge the constructive suggestions by Chen Ji, an anonymous reviewer, and the guest editor Brad Aagaard. We are grateful to Stefano Pintore who digitized the Presidio marigram by means of the Teseo software (Pintore et al., 2005). Some figures have been drawn with Generic Mapping Tools (Wessel and Smith, 1998).

References

Beresnev, I. A. (2003). Uncertainties in finite-fault slip inversions: to what extent to believe? (a critical review), *Bull. Seismol. Soc. Am.*, **93**, no. 6, 2445-2458.

Bowditch, N. (1966). *American practical navigator.* U.S. Navy, Hydrographic Office, Washington, D.C., 524 p.

Divins, D. L., and D. Metzger. NGDC Coastal relief model, *Retrieved data goes here*, http://www.ngdc.noaa.gov/mgg/. National Geophysical Data Center, National Oceanic & Atmospheric Administration, U. S. Department of Commerce.

Disney, L. P., and W. H. Overshiner (1925). *Tides and currents in San Francisco Bay.* U. S. Department of Commerce, U.S. Coast and Geodetic Survey, Special Publication 115, 125 p.

Duman, T. Y., O. Emre, A. Dogan, and S. Ozalp (2005). Step-over and bend structures along the 1999 Duzce earthquake surface rupture, North Anatolian fault, Turkey, *Bull. Seismol. Soc. Am.*, **95**, no. 4, 1250-1262.

Fujii, Y., and K. Satake (2006), Source of the July 2006 West Java tsunami estimated from tide gauge records, *Geophys. Res. Lett.*, **33**, L24317, doi 10.1029/2006GL028049.

Fujii, Y., and K. Satake (2007). Tsunami source of 2004 Sumatra-Andaman earthquake inferred from tide-gauges and satellite data, *Bull. Seismol. Soc. Am.*, **97**, no. 1A, S192–S207.

Geist, E. (1999). Local tsunamis and earthquake source parameters, *Advances in Geophysics*, **39**, 117-209.

Geist, E. (2002). Complex earthquake rupture and local tsunamis, *J. Geophys. Res.*, **102**, B5, 2086, doi 10.1029/2000JB000139.

Geist, E. L., and M. L. Zoback (1999). Analysis of the tsunami generated by the M 7.8 1906 San Francisco earthquake, *Geology*, **27**, no. 1, 15-18.

Geist, E. L., and M. L. Zoback (2002). Examination of the tsunami generated by the 1906 San Francisco Mw = 7.8 earthquake, using new interpretations of the offshore San Andreas fault, in *Crustal Structure of the Coastal and Marine San Francisco Bay Region, California,* T. Parsons (ed.), *U.S. Geol. Surv. Prof. Paper 1658*, 29-42.

Grinsted, A., S. Jevrejeva, and J. Moore (2004). Application of the cross wavelet transform and wavelet coherence to geophysical time series. In the special issue: Nonlinear analysis of multivariate geoscientific data - advanced methods, theory and application. *Nonlinear Proc. Geophys.*, **11**, 561-566.

Ji, C., D. J. Wald, and D. V. Helmberger (2002). Source description of the 1999 Hector Mine, California earthquake; Part I: wavelet domain inversion theory and resolution analysis, *Bull. Seismol. Soc. Am.*, **92**, no. 4, 1192-1207.

Johnson, J. M., K. Satake, S. R. Holdahl, and J. Sauber (1996). The 1964 Prince Williams Sound earthquake; joint inversion of tsunami and geodetic data, *J. Geophys. Res.* **101**, B1, 523–532, doi 10.1029/95JB02806.

Kenner, S., and P. Segall (2003). Lower crustal structure in Northern California: implications from strain-rate variations following the 1906 San Francisco earthquake, *J. Geophys. Res.*, **108**, B1, 2011, doi 10.1029/2001JB000189

Lawson, A. C., chairman (1908). *The California earthquake of April 18, 1906, Report of the State Earthquake Investigation Commission*, Carnegie Institution of Washington Publication 87, 2 volumes, (reprinted 1969).

Liu, P., and R. J. Archuleta (2004). A new nonlinear finite fault inversion with three-dimensional Green's functions: application to the 1989 Loma Prieta, California, earthquake, *J. Geophys. Res.*, **109**, B0, 2318, doi 10.1029/2003JB002625.

Lomax, A. (2007). Location of the Focus and Tectonics of the Focal Region of the California Earthquake of 18 April 1906, *Bull. Seism. Soc. Am.,* **this issue**

Ma, K. F., K. Satake, and H. Kanamori (1991). The origin of the tsunami excited by the 1906 San Francisco earthquake, *Bull. Seism. Soc. Am.,* **81**, no. 4, 1396–1397.

Mader, C. L. (2001). *Numerical modeling of water waves,* Los Alamos series in Basic and Applied Sciences, 206 p.

Mosegaard, K., and A. Tarantola (1995). Monte Carlo sampling of solutions to inverse problems, *J. Geophys. Res.*, **100**, B7, 12,431-12,448, doi 10.1029/94JB03097.

Okada, Y. (1992). Internal deformation due to shear and tensile faults in a half-space, *Bull. Seismol. Soc. Am.*, **82**, no. 2, 1018-1040.

Ortiz, M. and Bilham R. (2003). Source area and rupture parameters of the 31 December 1881 M_W=7.9 Car Nicobar earthquake estimated from tsunamis recorded in the Bay of Bengal, *J. Geophys. Res.*, **108** (4), doi 10.1029/2002JB001941.

Parsons, T., and P. E. Hart (1999). Dipping San Andreas and Hayward faults revealed beneath San Francisco Bay, California, *Geology,* **27**, no. 9, 839-842.

Parsons, T., J. McCarthy, P. E. Hart, J. A. Hole, J. Childs, D. H. Oppenheimer, and M. L. Zoback (2002). A Review of faults and crustal structure in the San Francisco Bay area as revealed by seismic studies: 1991-97, in *Crustal Structure of the Coastal and Marine, San Francisco Bay Region, California*, T. Parsons (ed.), *U.S. Geol. Surv. Professional Paper 1658, 119-145.*

Parsons, T., R. Sliter, E. L. Geist, R. C. Jachens, B. E. Jaffe, A. Foxgrover, P. E. Hart, and J. McCarthy (2003), Structure and Mechanics of the Hayward–Rodgers Creek Fault Step-Over, San Francisco Bay, California, *Bull. Seismol. Soc. Am.*, **93**, no. 5, 2187-2002.

Piatanesi, A., S. Tinti, and I. Gavagni (1996). The slip distribution of the 1992 Nicaragua earthquake from tsunami run-up data, *Geophys. Res. Lett.*, **23** (1), 37-40, doi 10.1029/95GL03606.

Piatanesi A., and S. Lorito (2007). Rupture Process of the 2004 Sumatra-Andaman Earthquake from Tsunami Waveform Inversion, *Bull. Seism. Soc. Am.*, **97**, no. 1A, S223–S231.

Pintore, S., M. Quintiliani, and D. Franceschi (2005). Teseo: a vectoriser of historical seismograms. *Computer and Geosciences*, **31**, no. 10, 1277-1285.

Rabinovich, A. (1997). Spectral analysis of tsunami waves: Separation of source and topography effects, *J. Geophys. Res.*, **102** (C6), 12,663-12,676, 10.1029/97JC00479.

Rothman, D. (1986). Automatic estimation of large residual statics corrections, *Geophysics*, **51**, no. 2, 332-346.

Sambridge, M., and K. Mosegaard (2002). Monte Carlo methods in geophysical inverse problems, *Rev. Geophys.*, **40** (3), doi 10.1029/2000RG000089.

Satake, K. (1987). Inversion of tsunami waveforms for the estimation of a fault heterogeneity: method and numerical experiments, *J. Phys. Earth*, **35**, 241-254.

Sen, M., and P. L. Stoffa (1991). Nonlinear one-dimensional seismic waveform inversion using simulated annealing, *Geophysics*, **56**, n. 10, 1624-1638.

Song, S-G., G. Beroza, and P. Segall. (2007). A unified source model for the 1906 San Francisco earthquake, *Bull. Seism. Soc. Am.*, **this issue**.

Spudich, P., and D. P. Miller (1990). Seismic site effects and the spatial interpolation of earthquake seismograms: results using aftershocks of the 1986 North Palm Springs, California earthquake, *Bull. Seismol. Soc. Am.*, **80**, no. 6, 1504-1532.

Spudich, P., M. Guatteri, K. Otsuki, and J. Minagawa (1998). Use of fault striations and dislocation models to infer tectonic shear stress during the 1995 Hyogo-Ken Nanbu (Kobe) earthquake, *Bull. Seism. Soc. Am.*, **88**, no. 2, 413-427.

Steacy, S., J. Gomberg, and M. Cocco (2005). Introduction to special section: Stress transfer, earthquake triggering, and time-dependent seismic hazard, *J. Geophys. Res.*, **110**, B05S01, doi 10.1029/2005JB003692.

Thatcher, W., G. Marshall, and M. Lisowski (1997). Resolution of fault slip along the 470-km-long rupture of the great 1906 San Francisco earthquake and its implications, *J. Geophys. Res.*, **102,** B3, 5,353-5,367, doi 10.1029/96JB03486.

Torrence, C., and G.P. Compo (1998). A practical guide to wavelet analysis, *Bull. Am. Meteorol. Soc.*, **79**, no. 1, 61-78.

Wald, D.J., H. Kanamori, D. V. Helmberger, and T. H. Heaton (1993). Source Study of the 1906 San Francisco Earthquake, *Bull. Seism. Soc. Am.*, **83**, no. 4, 981-1019.

Ward, S. N. (2000). San Francisco Bay Area Earthquake Simulations: A Step Toward a Standard Physical Earthquake Model. *Bull. Seism. Soc. Am.*, **90**, no. 2, 370-386.

Wessel, P. and W. H. F. Smith (1998). New, improved version of the Generic Mapping Tools released, *EOS Trans. AGU,* **79** (47), 579, doi 10.1029/98EO00426.

Zoback, M. L., R. C. Jachens and J. A. Olson (1999). Abrupt along strike change in the tectonic style: San Andreas fault zone, San Francisco Peninsula, J. Geophys. Res., **104**, B5, 10, 719-10,742, doi 10.1029/1998JB900059 .

Figure Captions

Figure 1

Bathymetry and coastlines in the calculation domain for tsunami simulations. Depths are plotted as a gray scale image according to the color scale. Thick straight lines are vertical surface projections of the upper edge of the three fault structures considered in this study (NWSAF, WSF and SFP). Thin gray lines are vertical projections of the lower and lateral edges of the faults. Thin black lines indicate margins between subfaults (numbered from 1 to 12). Gray triangles indicate centers of the upper edge of each subfault. The black star shows the position of the Presidio tide-gage.

Figure 2

The marigram recorded at the Presidio tide-gage on the 18th of April, 1906. Modified after Lawson (1906).

Figure 3

Detrended 1906 Presidio marigram (bottom panel). The record shown starts at 2 hours before the earthquake origin time. In the top panel is plotted in grey scale the squared modulus of the marigram wavelet transform (spectral power). Horizontal scale is time in minutes after the earthquake origin time. Vertical scale measures spectral periods in minutes. The dashed line delimits the cones of influence of the time series edges. Only the values of the power spectrum in the time-period region below the dashed line are reliable. Thick black contours delimit the 95% confidence level against red noise.

Figure 4

Tsunami travel times from the Presidio tide-gage, calculated in the linear long-waves shallow-water approximation with phase velocity $c=sqrt(gh)$ where g is gravitational acceleration and h water depth. Contour lines are at 1 minute intervals. Rectangular surfaces (thick line along top edge) show the three fault structures considered in this study (NWSAF, WSF and SFP).

Figure 5

Static, vertical displacement corresponding to a slip of 5 m on NWSAF, 1 m on WSF and 4 m on SFP. Countours are at 2 cm intervals, continuous lines correspond to positive displacement while dashed lines to negative displacement (subsidence).

Figure 6

Water height as a function of time after the earthquake at the Presidio tide gauge. Compared are the detrended Presidio marigram (continuous curve) and three simulated marigrams, as they result by forward modeling of the 1906 earthquake (dashed curves). See text for details on the source parameters for each of the cases.

Figure 7

Simulated marigram at the Presidio tide-gage coordinates, calculated in both of the cases with the same source parameters, but in one case with the seismic source as a whole (continuous) while in the other case as a linear combination of the Green's functions (dashed).

Figure 8

The complete set of results the synthetic inversion test case. a) Target, noisy marigram (grey continuous), best model (grey dashed) and the set of "good models" with lower cost functions values (see text for details). b) Circles are target (imposed) slip values on the 12 subfaults; crosses (connected by a dashed line) are the slip values retrieved after the inversion, with 1 σ error bars corresponding to the good models in a). The error bars associated with intermediate subfaults 2 to 5 are obtained by linear interpolation of those associated to the terminals 1 and 6; error bars 9 to 11 by those of 8 and 12. c) Marginal distributions for each of the inverted parameters, along with the best model value (vertical black lines).

Figure 9

Comparison between the detrended 1906 marigram and best models resulting from nonlinear inversions, with: a) SFP dip angle of 75°; b) SFP dip angle of 90°.

Figure 10

Comparison between the detrended 1906 marigram and best models resulting from nonlinear inversions, with: a) delayed rupture initiation on both SFP and NWSAF; b) delay of rupture initiation allowed on NWSAF only.

Figure 11

The complete set of results the 1906 Presidio marigram inversion. a) detrended Presidio marigram (grey continuous), best model (grey dashed) and the set of "good models" with lower cost functions values (see text for details). b) crosses (connected by a dashed line) are the slip values retrieved after the inversion, with 1 σ error bars corresponding to the good models in a). The error bars associated with intermediate subfaults 2 to 5 are obtained by linear interpolation of those associated to the terminals 1 and 6; error bars 9 to 11 by those of

8 and 12. c) Marginal distributions for each of the inverted parameters, along with the best model value (vertical black lines).

Figure 12

Static, vertical displacement corresponding to slip values listed in table 1 and corresponding to the best model. Contours are at 2 cm intervals, continuous lines correspond to positive displacement while dashed lines to negative displacement (subsidence).

Table 1

Subfault parameters

Fault segment	LONG.(*) E	LAT.(*) N	W (km)	L (km)	Strike (deg)	Rake (deg)	Dip (deg)	Top (km)	Best Model Slip (m)
1 NWSAF	-122.91627	38.183185	9	75	145	180	90	1	5.7±0.3
2 NWSAF	-122.65384	37.888513	9	5	145	180	90	1	5.1±0.3(***)
3 NWSAF	-122.62110	37.851679	9	5	145	180	90	1	4.4±0.3(***)
4 NWSAF	-122.58838	37.814845	9	5	145	180	90	1	3.7±0.4(***)
5 NWSAF	-122.55568	37.778011	9	5	145	180	90	1	3.0±0.4(***)
6 NWSAF	-122.52298	37.741176	9	5	145	180	90	1	2.3±0.5
7 WSF	-122.52430	37.736200	7.72	8	168	270	65	3	0.0±0.3
8 SFP	-122.51971	37.700768	9.32	5	146	180	75 or 90	1	0.0±0.3
9 SFP	-122.48801	37.663489	9.32	5	146	180	75 or 90	1	1.0±0.2(***)
10 SFP	-122.45632	37.626211	9.32	5	146	180	75 or 90	1	2.0±0.2(***)
11 SFP	-122.42464	37.588932	9.32	5	146	180	75 or 90	1	3.0±0.1(***)
12 SFP	-122.17173	37.290704	9.32	75	146	180	75 or 90	1	4(**)

(*) Longitude and latitude refer to the central point on upper edge of each subfault.

(**) Fixed a-priori.

(***) Slip value and errors are obtained by linear interpolation of the slip on the fault segment terminals.

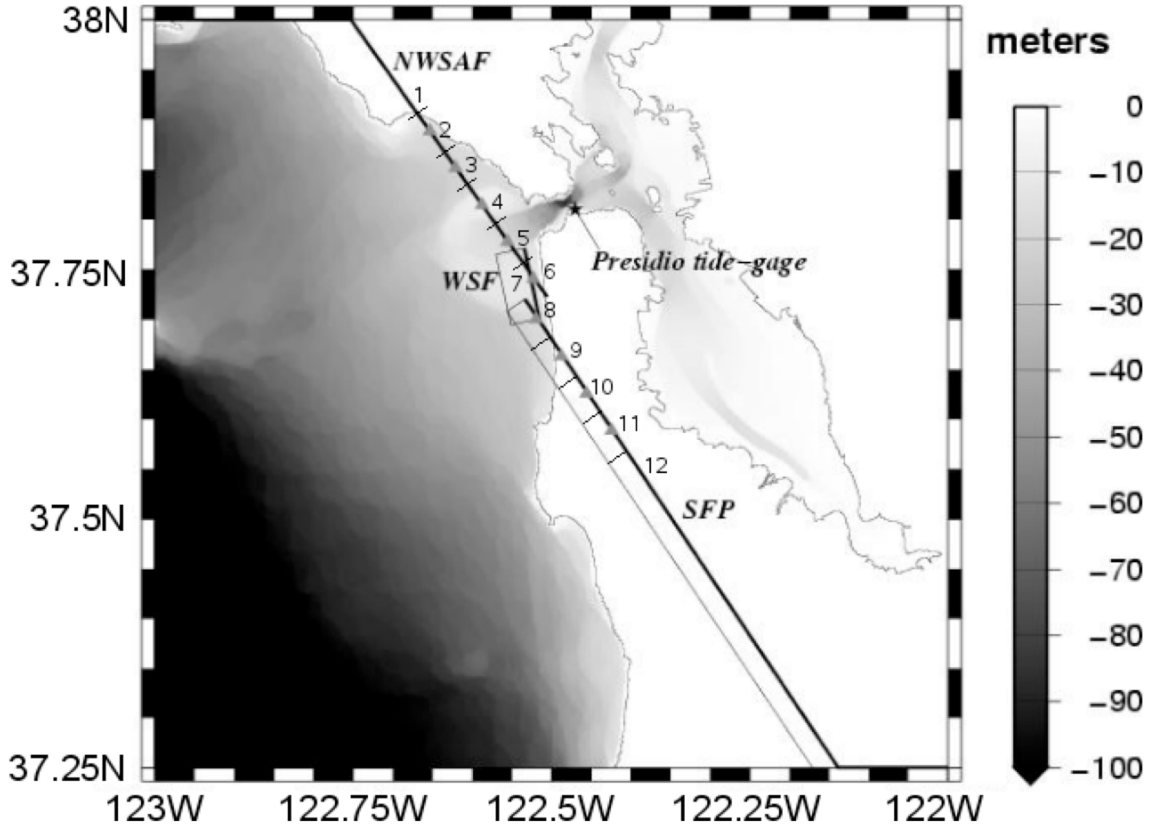

FIGURE 1, ms#2006412, Lorito, ↑up, 1 COLUMN

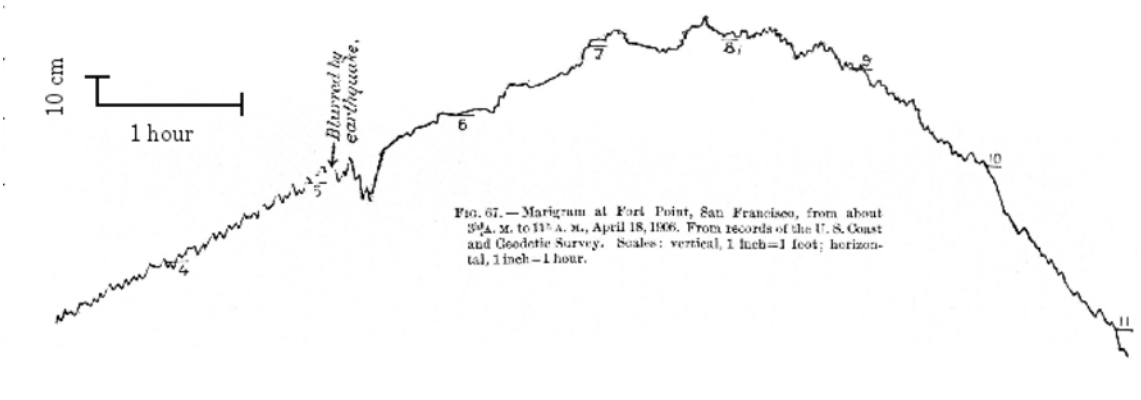

FIG. 67.—Marigram at Fort Point, San Francisco, from about 5½ A. M. to 11½ A. M., April 18, 1906. From records of the U. S. Coast and Geodetic Survey. Scales: vertical, 1 inch=1 foot; horizontal, 1 inch=1 hour.

720 FIGURE 2, ms#2006412, Lorito, ↑up, 2 COLUMNS

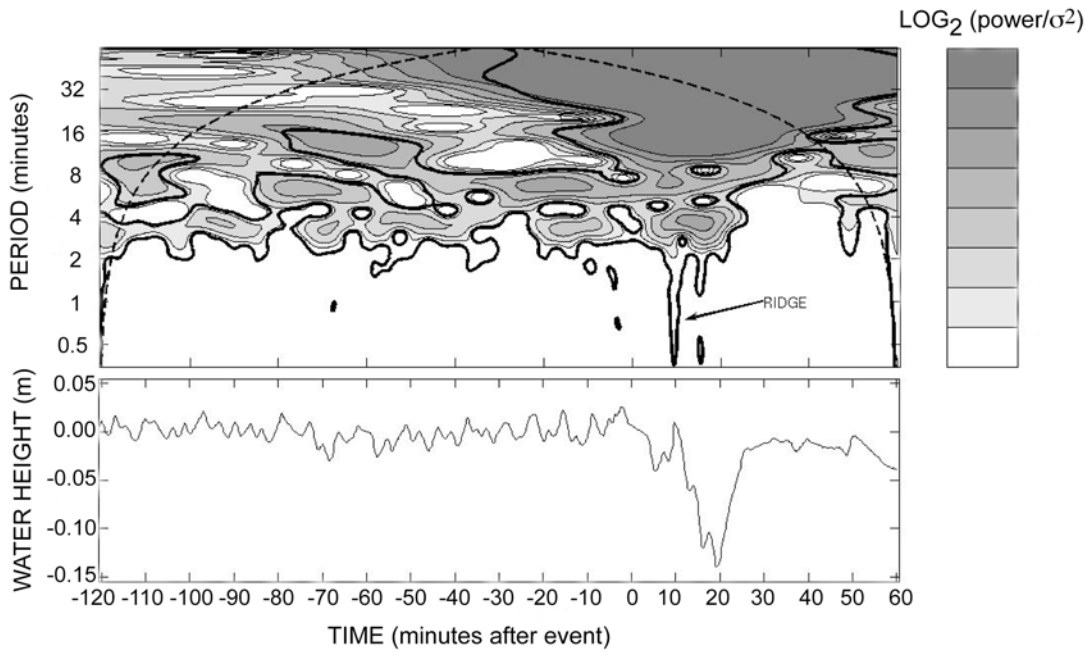

725

FIGURE 3, ms#2006412, Lorito, ↑up, 2 COLUMNS

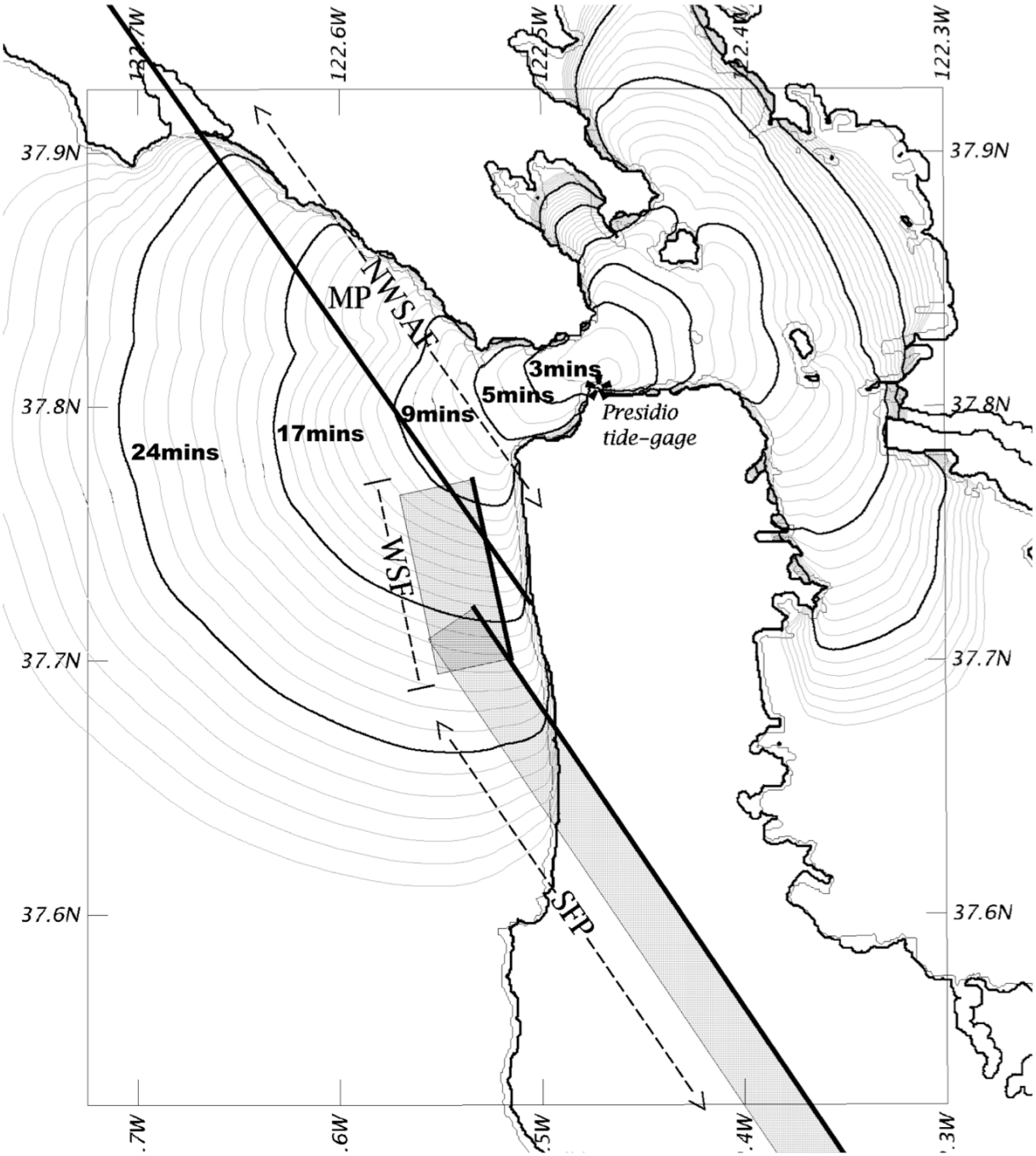

730

FIGURE 4, ms#2006412, Lorito, ↑up, 1 COLUMN

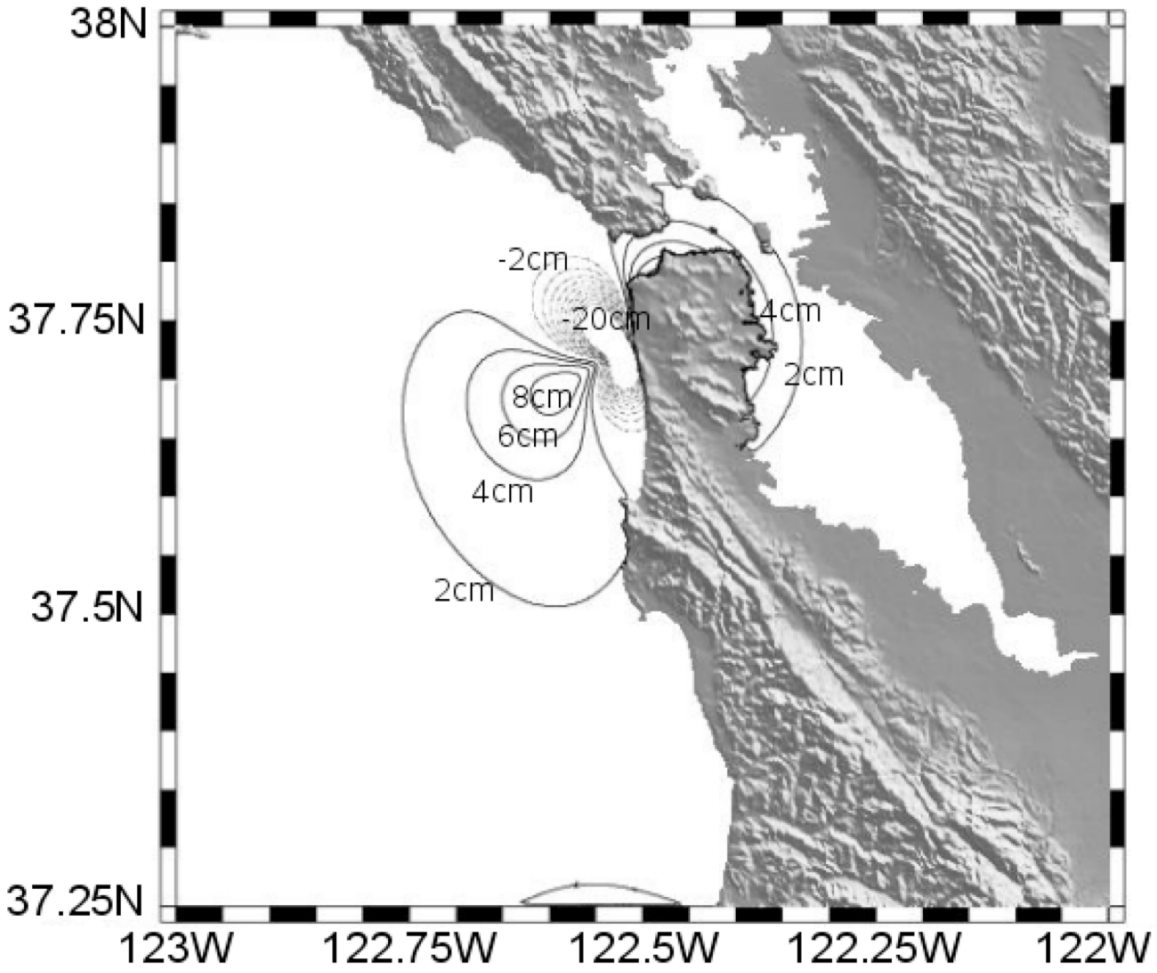

735

740 FIGURE 5, ms#2006412, Lorito, ↑up, 1 COLUMN

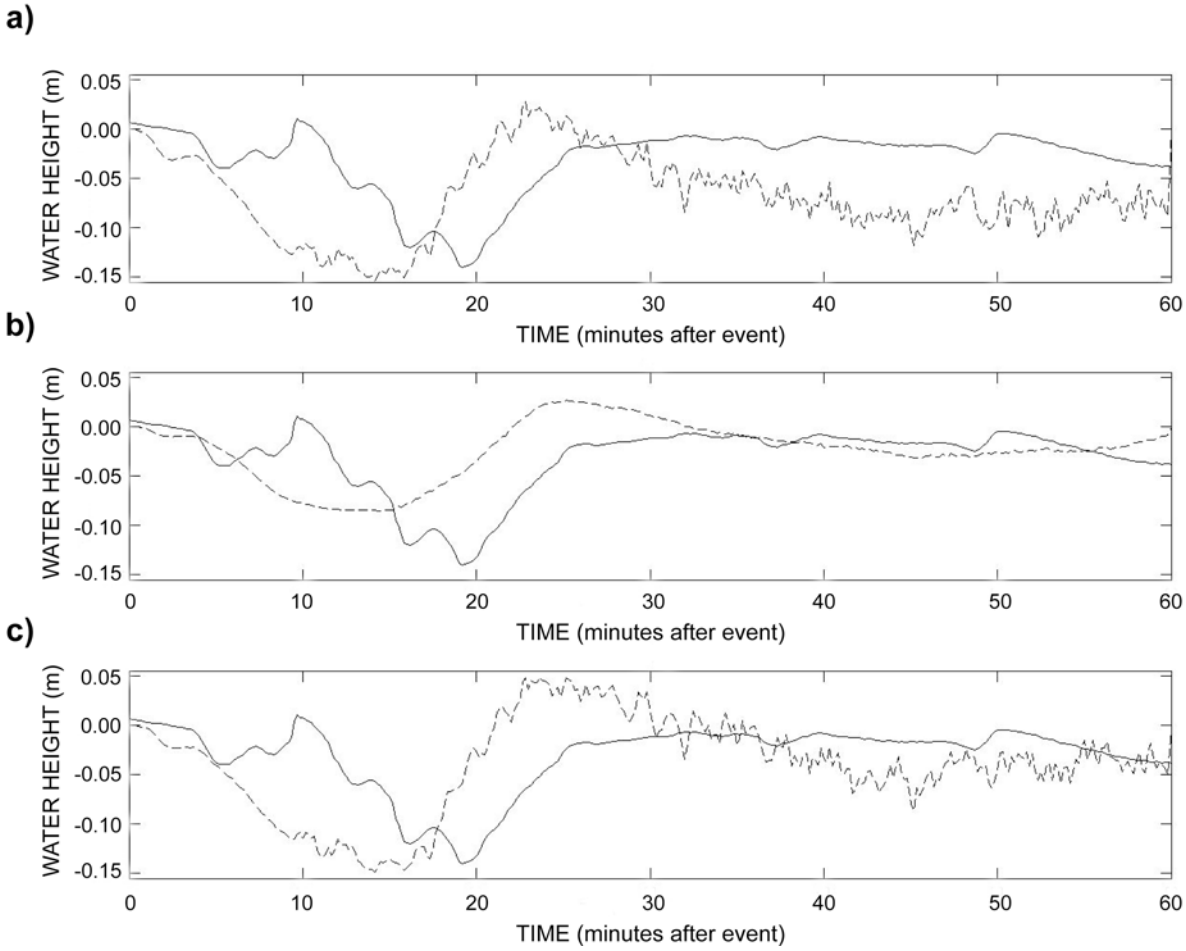

745

FIGURE 6, ms#2006412, Lorito, ↑up, 2 COLUMNS

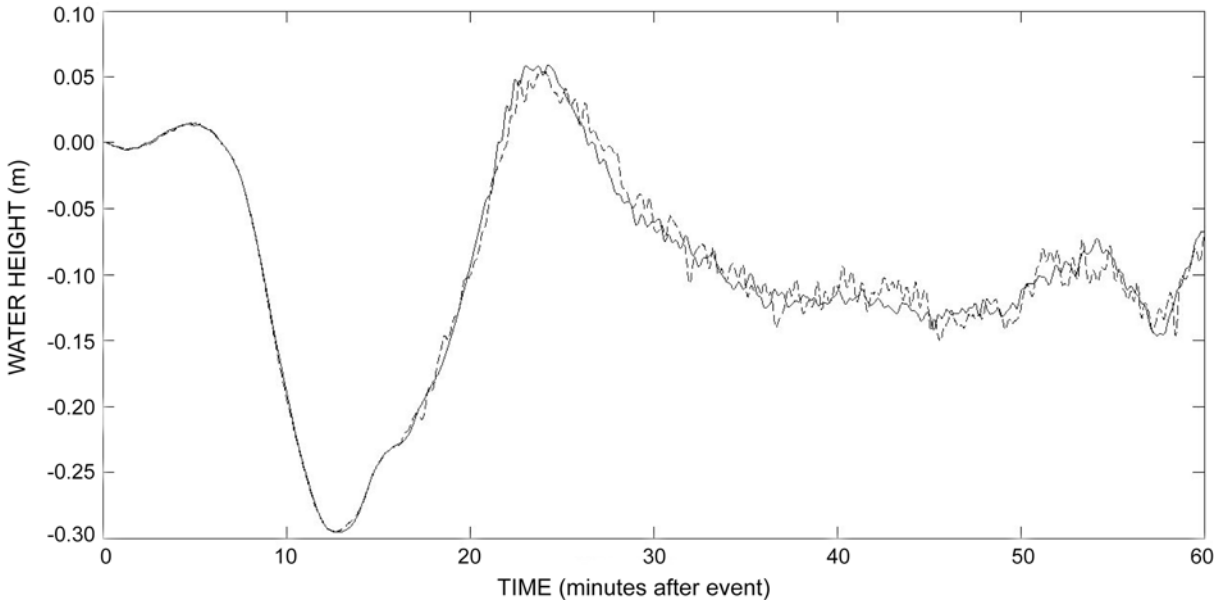

750

FIGURE 7, ms#2006412, Lorito, ↑up, 2 COLUMNS

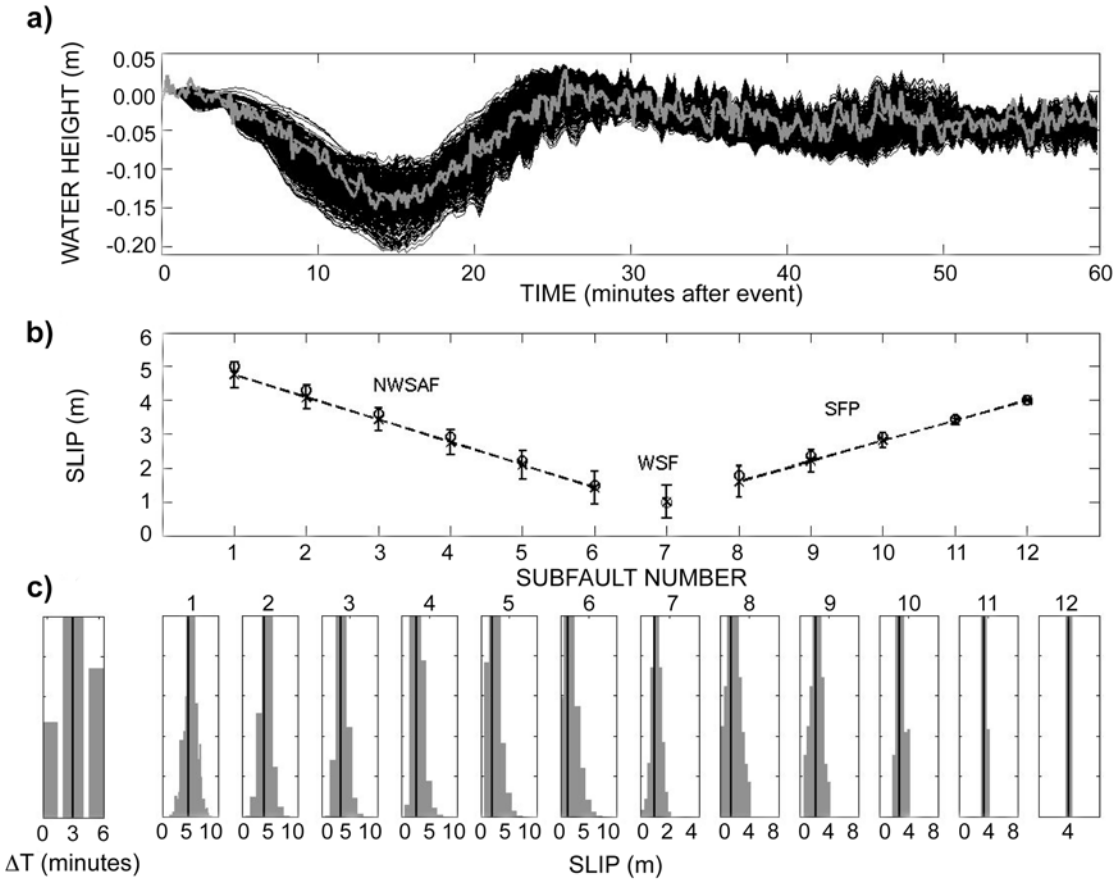

755

FIGURE 8, ms#2006412, Lorito, ↑up, 2 COLUMNS

760

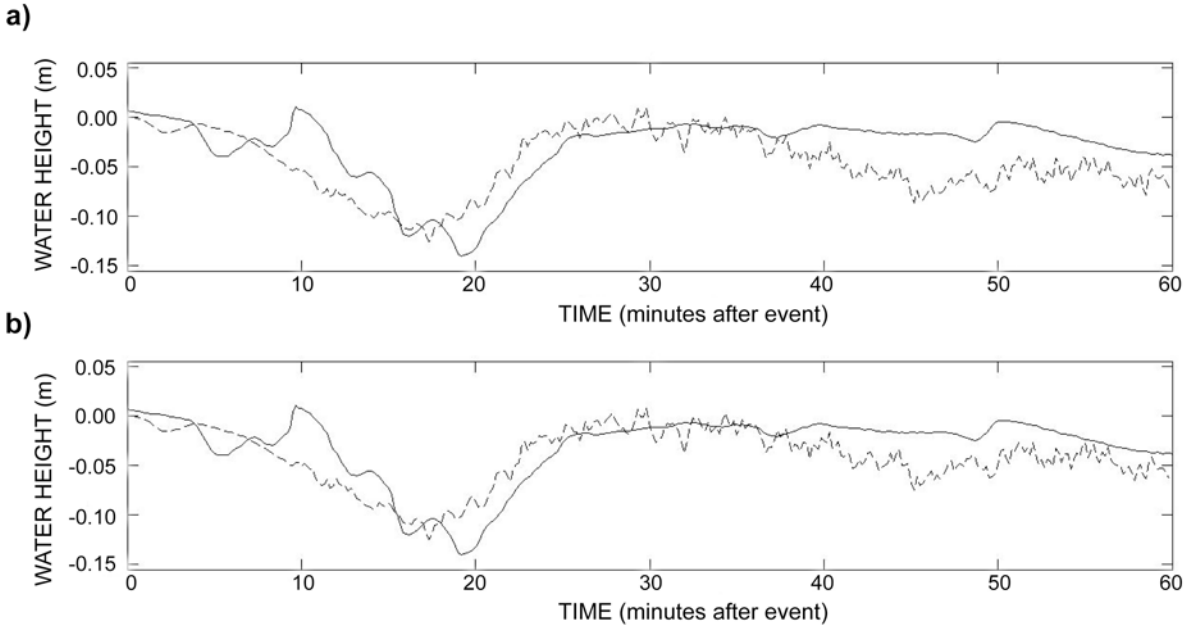

760

FIGURE 9, ms#2006412, Lorito, ↑up, 2 COLUMNS

765

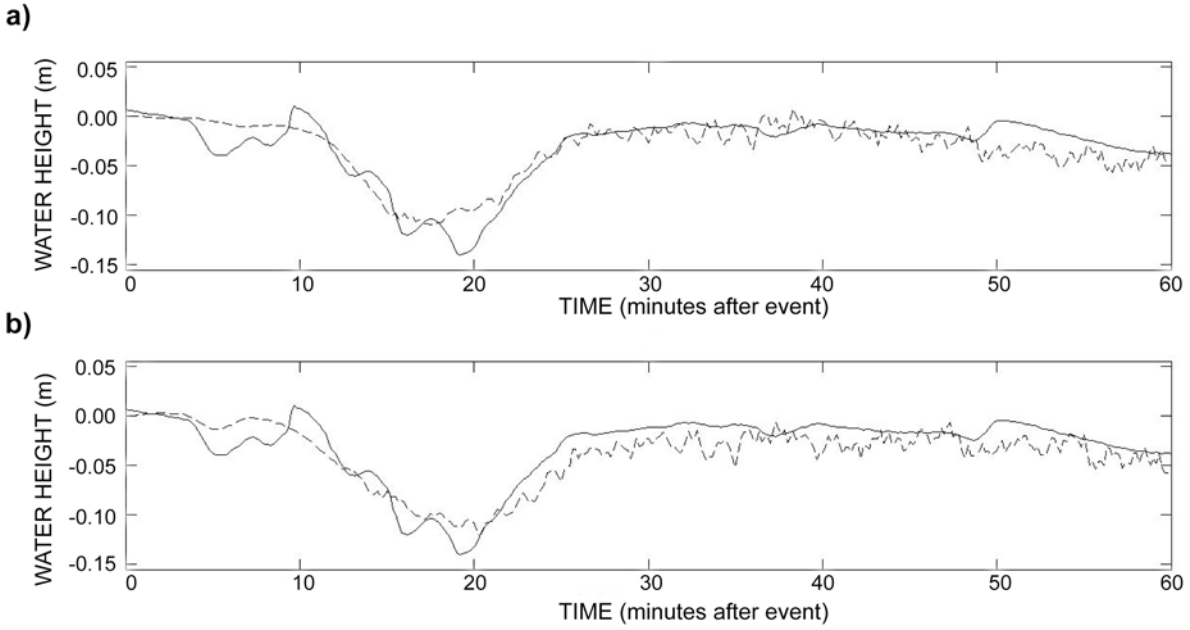

770 FIGURE 10, ms#2006412, Lorito, ↑up, 2 COLUMNS

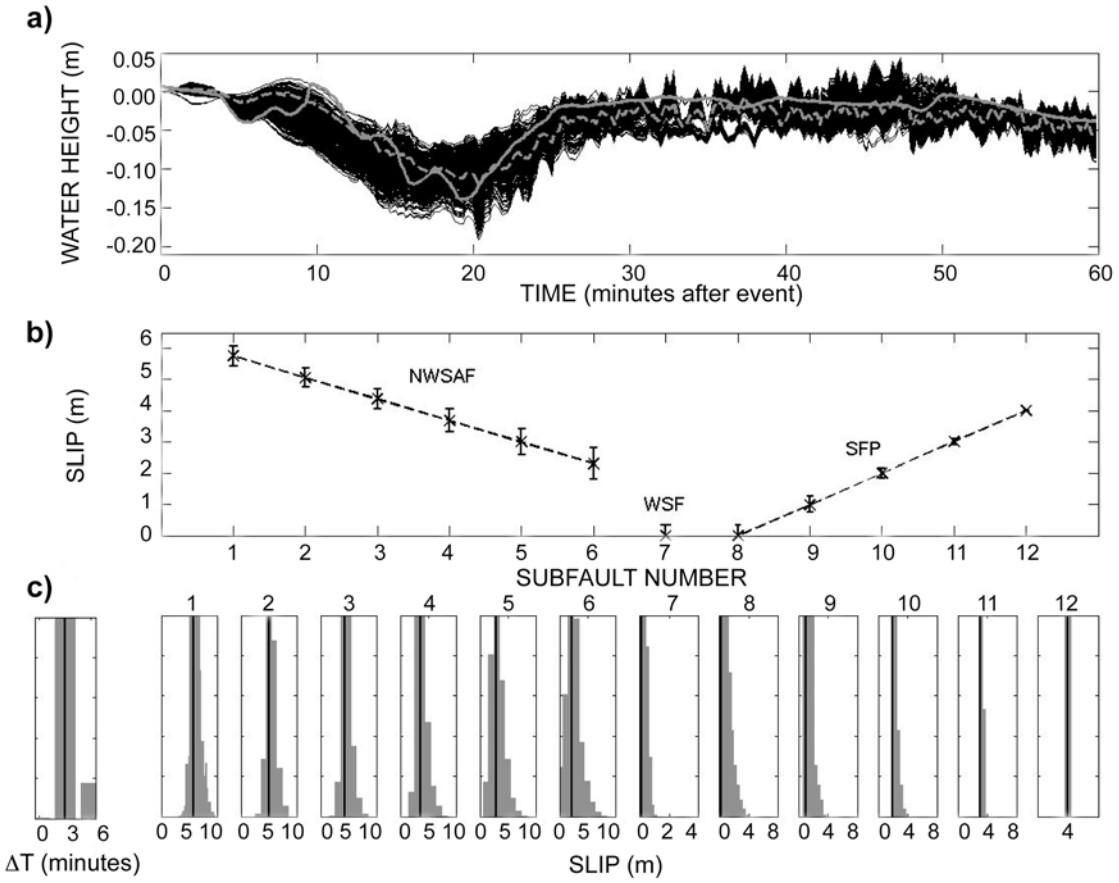

775

FIGURE 11, ms#2006412, Lorito, ↑up, 2 COLUMNS

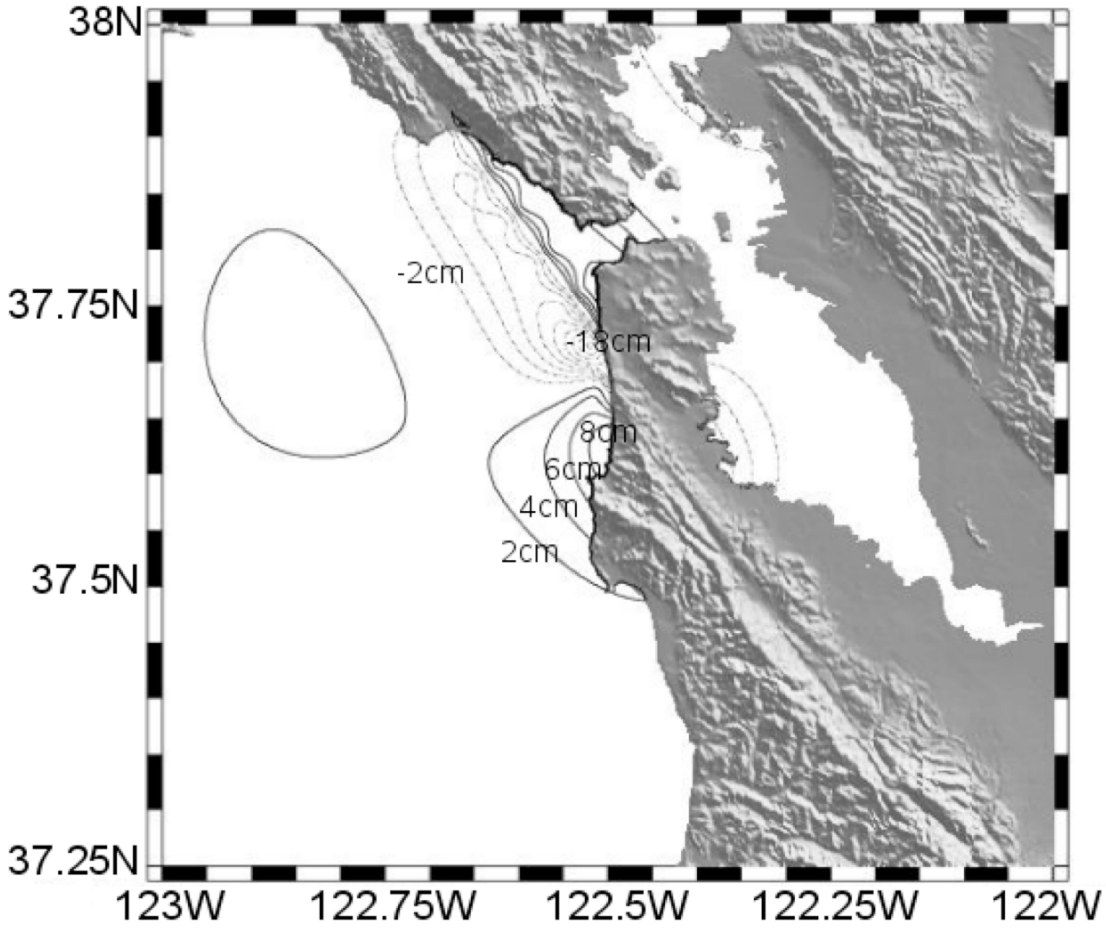

780

FIGURE 12, ms#2006412, Lorito, ↑up, 1 COLUMN